

Intermolecular interactions and substrate effects for an adamantane monolayer on the Au(111) surface

Yuki Sakai,^{1,2} Giang D. Nguyen,² Rodrigo B. Capaz,^{2,3} Sinisa Coh,^{2,4}
 Ivan V. Pechenezhskiy,^{2,4} Xiaoping Hong,² Feng Wang,^{2,4} Michael
 F. Crommie,^{2,4} Susumu Saito,¹ Steven G. Louie,^{2,4} and Marvin L. Cohen^{2,4}

¹*Department of Physics, Tokyo Institute of Technology,
 2-12-1 Oh-okayama, Meguro-ku, Tokyo 152-8551, Japan*

²*Department of Physics, University of California, Berkeley, California 94720, USA*

³*Instituto de Fisica, Universidade Federal do Rio de Janeiro,
 Caixa Postal 68528, Rio de Janeiro, RJ 21941-972, Brazil*

⁴*Materials Sciences Division, Lawrence Berkeley
 National Laboratory, Berkeley, California 94720, USA*

(Dated: November 9, 2018)

Abstract

We study theoretically and experimentally the infrared (IR) spectrum of an adamantane monolayer on a Au(111) surface. Using a new STM-based IR spectroscopy technique (IRSTM) we are able to measure both the nanoscale structure of an adamantane monolayer on Au(111) as well as its infrared spectrum, while DFT-based ab initio calculations allow us to interpret the microscopic vibrational dynamics revealed by our measurements. We find that the IR spectrum of an adamantane monolayer on Au(111) is substantially modified with respect to the gas-phase IR spectrum. The first modification is caused by the adamantane–adamantane interaction due to monolayer packing and it reduces the IR intensity of the 2912 cm^{−1} peak (gas phase) by a factor of 3.5. The second modification originates from the adamantane–gold interaction and it increases the IR intensity of the 2938 cm^{−1} peak (gas phase) by a factor of 2.6, and reduces its frequency by 276 cm^{−1}. We expect that the techniques described here can be used for an independent estimate of substrate effects and intermolecular interactions in other diamondoid molecules, and for other metallic substrates.

I. INTRODUCTION

Diamondoids form a class of hydrocarbon molecules composed of sp^3 hybridized carbon atoms. They can be regarded as small pieces of diamond whose dangling bonds are terminated with hydrogen atoms. Diamondoids are known to exhibit negative electron affinity and they have possible applications as electron emitters,^{1,2} and other nanoscale devices.³ Diamondoids have also attracted much interest because of their possible appearance in the interstellar medium.^{4,5} The smallest diamondoid is adamantane ($C_{10}H_{16}$), which has a highly symmetric cage-like structure (T_d point group) illustrated in Fig. 1(a). Various theoretical and experimental results on infrared (IR) spectroscopy of both gas and solid adamantane have been reported in the literature.^{5–13} Self-assembled monolayers of larger diamondoids than adamantane (i. e. tetramantane) on a Au(111) surface system has been studied with scanning tunneling microscopy (STM).^{3,14} The infrared spectrum of a functionalized adamantane on a Au(111) surface has been studied in Ref. 15; however the functionalization prevents adamantane molecules from being in direct contact with the Au(111) surface. Therefore a detailed characterization of the adamantane monolayer–gold surface interaction is missing.

In this work we investigate a submonolayer of adamantane in direct contact with a Au(111) surface. We experimentally obtained the IR spectrum of a self-assembled adamantane island on a Au(111) surface by using a newly developed method which combines infrared spectroscopy and scanning tunneling microscopy.¹⁴ The observed spectrum of the adamantane monolayer on Au(111) is significantly altered with respect to the gas and solid phase of adamantane. To account for this difference theoretically, we studied the IR spectrum within the framework of density functional theory (DFT) and density functional perturbation theory (DFPT). Our analysis reveals that intermolecular and molecule-substrate interactions cause mixing (hybridization) of the gas phase vibrational modes. As a result, IR-active vibrational modes of adamantane molecules on a gold substrate are found to be considerably different than those of the gas phase. For example, our calculations show that the intermolecular interaction in the adamantane monolayer reduces the IR intensity of one of the gas-phase IR peaks by a factor of 3.5. In addition, the interaction between adamantane molecules and the Au(111) substrate increases the IR intensity of another gas-phase mode by a factor of 2.6 and causes a significant redshift of 276 cm^{-1} for this mode.

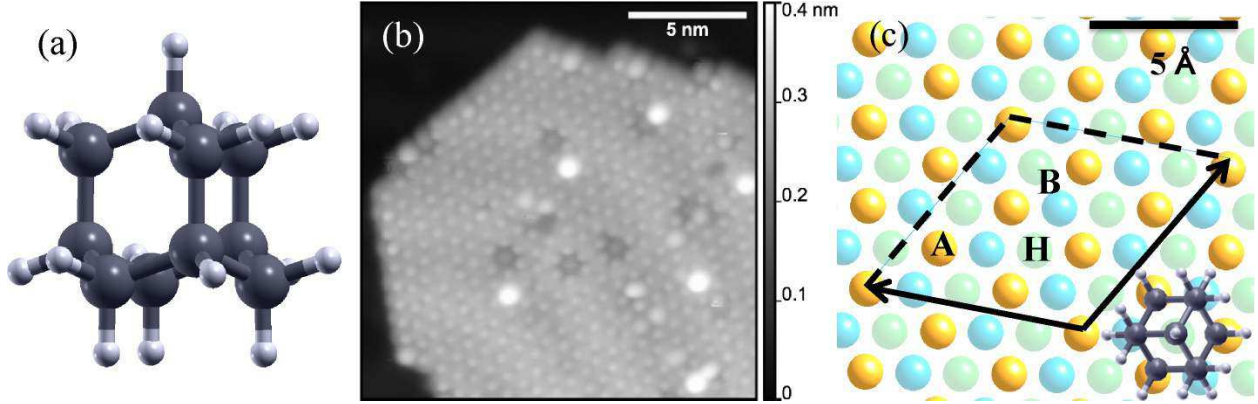


FIG. 1. (Color online) (a) Model of molecular structure of an adamantane molecule. Hydrogen and carbon atoms are represented by white and gray spheres, respectively. (b) STM topography of a self-assembled island of adamantane molecules on a Au(111) surface (sample bias $V_{\text{sample}} = -1.0$ V, current setpoint $I = 100$ pA, temperature $T = 13$ K). (c) Schematic picture of alignment of the molecules on the Au(111) surface. Gold atoms in the topmost layer, second layer, and third layer are represented by gold, blue, and green color spheres of different shades. Black lines show the supercell of the $\sqrt{7} \times \sqrt{7}$ molecular alignment. Upper case letters indicate the location of adsorption sites: A for *atop* site, B for *bridge* site, and H for *hollow* site. Top view of an adamantane in the hollow-atop geometry is also illustrated (the center of the molecule is in the *hollow* site and the three bottom hydrogen atoms are in the *atop* site.) The three bottom hydrogen atoms can be seen at the bottom of Fig. 1(a), but not be seen in Fig. 1(c)

This paper is organized as follows: in Sec. II, we describe the details of our experiment. In Sec. III we introduce the computational methods. In Sec. IV, we describe and analyze the theoretical and experimental IR spectra. In Sec. IV B 1, IV B 2 and IV B 3 we study theoretically the IR spectrum of a single adamantane molecule, the IR spectrum of an adamantane monolayer, and the IR spectrum of an adamantane monolayer on a Au(111) surface, respectively. In Sec. IV C we compare experimental and theoretical IR spectra. Finally, in Sec. V we discuss our conclusions.

II. EXPERIMENTAL SETUP

Adamantane (Sigma-Aldrich, purity $\geq 99\%$) was deposited onto a clean Au(111) surface from adamantane powder held in a vacuum chamber by exposing the gold surface to

adamantane vapor formed at room temperature. To achieve submonolayer molecule coverage the adamantane vapor flux was controlled with a leak valve. Before the deposition, it was necessary to precool a freshly cleaned gold crystal to 15 K to facilitate adsorption of the molecules onto the Au(111) surface. The precooled gold crystal was then transferred into a chamber with base pressure of $\sim 10^{-11}$ Torr where the crystal was held in a room temperature manipulator during the adamantane deposition which lasted for about ten minutes (pressure rose to $\sim 10^{-9}$ Torr when the adamantane valve was opened for deposition). After the deposition, the sample was immediately transferred into a homemade ultra-high vacuum variable temperature STM operating at $T = 13\text{--}15$ K for STM surface characterization. The adamantane molecules on Au(111) were observed to self-assemble into hexagonally packed molecular islands with a lattice constant of 7.5 ± 0.2 Å. Figure 1(b) shows a typical STM image of an adamantane island on a Au(111) surface.

IR absorption spectra of adamantane submonolayers on the Au(111) surface were obtained by using a recently developed technique referred to as infrared scanning tunneling microscopy (IRSTM).¹⁴ IRSTM employs an STM tip in tunneling mode as a sensitive detector to measure the thermal expansion of a sample due to molecular absorption of monochromatic IR radiation. The surface thermal expansion of the sample, recorded as a function of IR frequency, yields the IR molecular absorption spectrum. Frequency-tunable IR excitation of the samples was achieved by using a homemade tunable mode-hop-free laser source based on a singly resonant optical parametric oscillator.¹⁶ The detailed description of the IRSTM setup and the discussion of its performance are given elsewhere.¹⁴

III. THEORETICAL CALCULATIONS

In this section, we describe the computational methods used in this work.

A. Geometry of adamantane on Au(111)

We start with a discussion of the orientation of an adamantane monolayer on the Au(111) surface as shown in Fig. 1. Based on the STM topography shown in Fig. 1(b), we model the molecular arrangement on a Au(111) surface. In our model, the adamantane molecules are arranged in a $\sqrt{7} \times \sqrt{7}$ structure as shown in Fig. 1(c). The intermolecular distance in this

model is 7.40 Å, which is close to the observed intermolecular distance 7.5 ± 0.2 Å. In our calculations we place the adamantane molecules so that the three-fold axis of the molecule is perpendicular to the surface, with three bottom hydrogen atoms facing down toward the Au(111) surface. Because of its three-fold symmetry, this configuration is compatible with the hexagonal self-assembled island seen in the STM topography Fig. 1(b).

We determine the most stable adsorption geometry of adamantane by computing the total energy for various adsorption sites. We perform *ab initio* total energy calculations within the framework of DFT^{17,18} to understand the properties of an adamantane monolayer on a Au(111) surface. We use the local density approximation (LDA) for the exchange and correlation energy functionals based on the quantum Monte-Carlo results of Ceperley and Alder¹⁹ as parameterized by Perdew and Zunger.²⁰ Vanderbilt ultrasoft pseudopotentials²¹ are adopted in combination with a plane wave basis with cut off energies of 30 and 360 Ry for the wavefunctions and charge density, respectively. A Brillouin zone integration is done on an $8 \times 8 \times 1$ uniform k -grid. Gaussian smearing with a 0.01 Ry width is used for the calculation of metallic systems. We use the Quantum ESPRESSO package²² to perform DFT calculations. We also use XCrySDen²³ to visualize the results.

We model the Au(111) surface by a finite slab with a thickness of seven gold layers with seven gold atoms in each layer in a supercell geometry²⁴. The primitive unit cell of the slab includes one adamantane molecule. Therefore, in total the primitive unit cell contains 75 atoms. The width of the vacuum region is 15.5 Å.

Binding energies and molecule-surface distances of four different optimized geometries are listed in Table I. The name of each geometry is based on the position of the center of the molecule and the positions of the three bottom hydrogen atoms shown in Fig. 1(a). In the most stable geometry (hollow-atop) the center of the molecule is on the hollow site and three hydrogen atoms are close to the gold atoms in the topmost layer (see Fig. 1(c)). The calculated distance between the bottom hydrogen atoms and the gold surface is 2.29 Å after optimization of the atomic coordinates.

It is well known that LDA energy functionals do not correctly describe long-range interactions such as the van der Waals interaction. Thus we also cross-check our results with van der Waals density functionals (vdW-DFs).^{25–29} In particular, we use an improved version²⁶ of the nonlocal vdW correlation functional together with Cooper exchange²⁷. We optimize the four different structures to compare the energetics with those of the LDA. After the

TABLE I. Theoretical binding energies and surface-molecular distances of several adsorption geometries obtained within the LDA approximation. The binding energies in the Table are computed as the sum of the total energy of the gold slab and the isolated adamantane molecule minus the total energy of an adamantane adsorbed on a Au(111) surface system. The convention for the binding sites of Au(111) (*atop*, *bridge*, *hollow*) is as in Fig. 1(c). In our naming convention (for example *atop-bridge*), the first part (*atop*) represents the position of the center of the adamantane molecule, and second part (*bridge*) represents position of the three bottom hydrogen atoms of adamantane.

Geometry	Distance	Binding energy
	Å	meV/molecule
atop-bridge	2.25	379
atop-hollow	2.25	384
hollow-atop	2.29	490
hollow-hollow	2.32	355

structural optimization with a vdW functional, the hollow-atop geometry remains the most stable configuration although the binding energy differences are reduced compared to the LDA (the binding energy difference between the hollow-atop geometry and the atop-bridge geometry is reduced from 111 meV/molecule (in LDA) to 44 meV/molecule). In addition, the distance between the molecule and surface using the vdW functional is increased from 2.29 Å (in LDA) to 2.45 Å in the hollow-atop geometry. Since both of these changes are not large, we expect that the use of the vdW-DF functionals throughout this work does not qualitatively affect the computed IR spectra.

B. Phonon and IR intensity calculation

Next, we describe the methods with which we compute the frequency and infrared intensity of the adamantane vibration modes, in various environments (gas, monolayer, and on the Au(111) substrate).

For this purpose we use density functional perturbation theory as described in Ref. 30. All calculations are done only in the Brillouin zone center point (Γ). We define the phonon effective charge of the j^{th} phonon branch as

$$Q^\alpha(\omega_j) = \sum_{\beta,s} Z_s^{\alpha\beta} U_s^\beta(\omega_j). \quad (1)$$

Here \mathbf{Z} is the Born effective charge tensor, $\mathbf{U}(\omega_j)$ is the eigendisplacement vector, and ω_j is the phonon frequency of the j^{th} phonon branch. Cartesian vector components are represented by α and β , while s represents the atom index. The Born effective charge $Z_s^{\alpha\beta}$ is defined as the first derivative of the force F_s^β acting on an atom s with respect to the electric field E_α ,

$$Z_s^{\alpha\beta} = \frac{\partial F_s^\beta}{\partial E_\alpha}. \quad (2)$$

The IR intensity of the j^{th} phonon branch can be computed from the phonon effective charge³¹

$$I_{\text{IR}}(\omega_j) = \sum_{\alpha} |Q^\alpha(\omega_j)|^2. \quad (3)$$

Once we obtain the IR intensities $I_{\text{IR}}(\omega_j)$, we model the IR spectrum at any frequency ω by assuming a Lorentzian lineshape with a constant linewidth of 10 cm^{-1} (full width at half maximum). In general, all nine Cartesian components of the Born effective charge must be calculated to obtain the IR intensities. However, on the metallic surface, one can focus only on the components of the electric field perpendicular to the surface ($\alpha = z$).^{32–34}

To compute the Born effective charge, we use a finite-difference approximation of Eq. 2, and we apply the electric field using a saw-tooth like potential in the direction perpendicular to the slab (z). Therefore we can obtain the Born effective charge by dividing the force induced by the electric field (ΔF) with the strength of the electric field (E_z).

Using this method we calculate the IR spectra of a single molecule, of a molecular monolayer without a substrate, and of molecules on a Au(111) substrate. To track the changes in the IR spectrum due to intermolecular interaction and due to substrate effects, we perform the following interpolation procedure. We define an interpolated dynamical matrix \mathbf{D}_{int} and Born effective charge \mathbf{Z}_{int} between any two configurations A and B as

$$\begin{aligned} \mathbf{D}_{\text{int}} &= (1 - \lambda)\mathbf{D}_A + \lambda\mathbf{D}_B, \\ \mathbf{Z}_{\text{int}} &= (1 - \lambda)\mathbf{Z}_A + \lambda\mathbf{Z}_B. \end{aligned} \quad (4)$$

Here $\mathbf{D}_{\text{int}} = \mathbf{D}_A$ for $\lambda = 0$ and $\mathbf{D}_{\text{int}} = \mathbf{D}_B$ for $\lambda = 1$ and is continuously tuned from A to B for $0 < \lambda < 1$ (same for \mathbf{Z}_{int}). Diagonalizing \mathbf{D}_{int} for each λ and using interpolated \mathbf{Z}_{int} we obtain interpolated IR intensity for each λ with $0 < \lambda < 1$.

For the start and end configurations A and B, we use either no subscript, subscript M, or subscript Au to denote either an isolated molecule, molecules in an isolated molecular monolayer, or in a monolayer on a Au(111) substrate, respectively. We first interpolate the spectra from the isolated molecule phase to the monolayer phase (M) to determine the effect of the intermolecular interactions. Finally to estimate the effect of the molecule-substrate interactions we interpolate the spectrum of the monolayer phase (M) to the case of molecules on the gold substrate (Au).

In the interpolation procedure, we take into account only dynamical matrix elements of carbon and hydrogen atoms (neglecting the displacements of gold atoms). We find that the effect of gold atom displacements on vibrational frequencies is only 0.3 cm^{-1} and on the IR intensity less than 10%.

In addition to the interpolation method we also quantitatively analyze the similarity of eigendisplacement vectors between various configurations. We do this by computing the norm of the inner product $|\langle u_i^A | u_j^B \rangle|^2$ between i^{th} phonon eigendisplacement vector $\langle u_i^A |$ in configuration A, and j^{th} phonon eigendisplacement vector $|u_j^B\rangle$ in configuration B. We use the same subscript convention as for the interpolation procedure (Au, M, or no subscript for molecules on the substrate, the molecular monolayer, or single molecule case respectively). Since an adamantane molecule consists of 78 phonon modes, we simplify the analysis by only considering inner products between the 16 predominantly C–H stretching modes.

IV. RESULTS

This section is organized as follows. We present our experimentally obtained IR spectra of an adamantane submonolayer on a Au(111) surface in Sec. IV A. Next, in Sec. IV B we analyze theoretically obtained IR spectra. Finally, in Sec. IV C we compare theory and experiment.

A. Experimental IR spectra

Figure 2 shows an experimentally measured IRSTM spectrum (green line) of 0.8 ML of adamantane adsorbed on a Au(111) surface. The spectrum was obtained by measuring the STM Z-signal under constant-current feedback conditions while sweeping the IR excitation from 2840 cm^{-1} to 2990 cm^{-1} (the spectrum shown was averaged over 15 frequency sweeps and background-corrected by subtracting a linear fit to the estimated bare gold contribution to the spectrum). Two IR absorption peaks for adamantane/Au(111) can clearly be seen at 2846 ± 2 and $2912 \pm 1\text{ cm}^{-1}$ in Fig. 2. The other small peaks seen in Fig. 2 are not reproducible and thus we are not able to unambiguously relate them to the adamantane absorption. The black dashed lines in Fig. 2 show the IR peak positions of an adamantane molecule in the gas phase.¹³ Comparing the green curve and the black dashed line in Fig. 2, it is clear that the IR spectrum of adamantane on the Au(111) surface is considerably different from the gas phase spectrum.

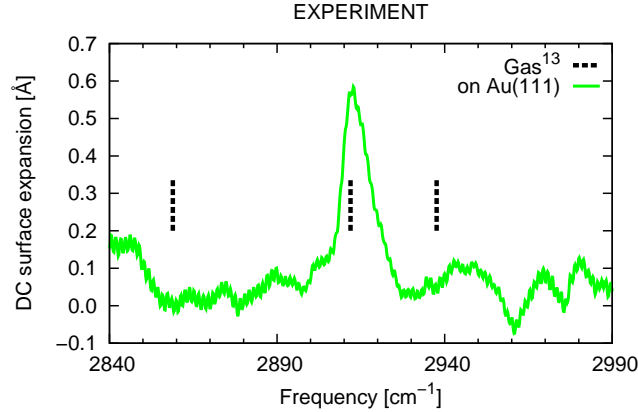


FIG. 2. (Color online) The green line shows the experimentally observed spectrum (averaged over 15 sweeps) of 0.8 ML of adamantane on a Au(111) surface with gold baseline signal subtracted. The IR absorption peaks are seen at 2846 ± 2 and $2912 \pm 1\text{ cm}^{-1}$. The vertical black dashed lines show the IR peak positions of an adamantane molecule in the gas phase as listed in Table II (2859, 2912, 2938 cm^{-1}).

TABLE II. Calculated vibrational frequencies (in cm^{-1}) and phonon effective charge Q^z (in elementary charge e) of an isolated adamantane molecule from 2850 cm^{-1} to 2950 cm^{-1} . Experimental values are shown for the gas phase¹³ and solution phase.¹⁰ We label phonon modes by ω_1 – ω_7 with one label corresponding to one irreducible representation (irrep). Only T_2 modes can be observed in the gas IR spectroscopy. A_1 , E , and T_2 are Raman active, while T_1 modes are inactive (both in IR and Raman).

	Irrep	Frequency	Q^z	Prev. experiment	
				Ref. 13 ^a	Ref. 10 ^b
ω_1	A_1	2924	-	-	2913
ω_2	A_1	2891	-	-	2857
ω_3	E	2892	-	-	2900
ω_4	T_1	2938	-	-	-
ω_5	T_2	2940	0.25	2938	2950
ω_6	T_2	2918	0.32	2912	2904
ω_7	T_2	2892	0.19	2859	2849

^a IR spectroscopy of gas phase adamantane.

^b IR and Raman spectroscopy of adamantane solution. Mode assignment is based on Ref. 11.

B. Theoretical analysis of IR spectra

To understand the origin of IR spectrum modification of adamantane on Au(111) we compute IR spectra for an isolated adamantane molecule, for an adamantane monolayer, and for an adamantane monolayer placed on the Au(111) substrate. We discuss these three cases in the following three subsections of the paper.

1. *Single molecule*

We compute the vibrational frequencies and IR intensities of an isolated single molecule of adamantane by placing the molecule in a large unit cell (length of each side is 16 Å) to minimize the interaction between periodic replicas. The calculated vibrational frequencies of the C–H bond stretching modes (and phonon effective charge) are listed in Table II and compared with the experimental frequencies from the literature.^{10,13} Our calculation reproduces quite well the vibrational frequencies as compared to the experimental data. We find the largest discrepancy of $\sim 30 \text{ cm}^{-1}$ for two modes (labeled ω_2 and ω_7 in Table II), while the discrepancy for the other modes is only $\sim 10 \text{ cm}^{-1}$.

There are 16 C–H stretching modes in adamantane (equal to the number of C–H bonds). Out of 16 modes, there are three modes corresponding to the T_2 irreducible representation, one T_1 , one E, and two A_1 modes. In the highly symmetric adamantane molecule (point group T_d) only these three T_2 modes are IR active while other C–H stretching modes are IR inactive. The IR active modes have the following approximate characters: asymmetric stretching of the C–H₂ bonds (labeled ω_5 in Table II), symmetric C–H stretch mode (ω_6), and symmetric C–H₂ stretch mode (ω_7). Their eigendisplacement vectors are also shown in Figs. 3(d), (e), and (f).

The calculated IR spectrum of an isolated adamantane molecule is indicated in Fig. 4 by a black dashed line. Here we compute only the $\alpha = z$ component of the IR intensities (Eq. 3) to simplify the comparison with the IR intensities of adamantane in molecular monolayer and monolayer on the Au(111) surface. We obtain three substantial IR absorption peaks of a single molecule adamantane in the frequency region from 2850 to 2950 cm^{-1} . The highest, middle, and lowest frequency peaks correspond to the ω_5 , ω_6 , and ω_7 modes, respectively. The ω_6 peak has the largest IR intensity, followed by the ω_5 peak. This order of the IR intensities is consistent with a previous DFT result¹².

2. *Adamantane monolayer*

Before analyzing the IR spectrum of an adamantane monolayer on a Au(111) surface, we first analyze the IR spectrum of a free adamantane monolayer (with the same intermolecular distance as in the monolayer on the gold substrate).

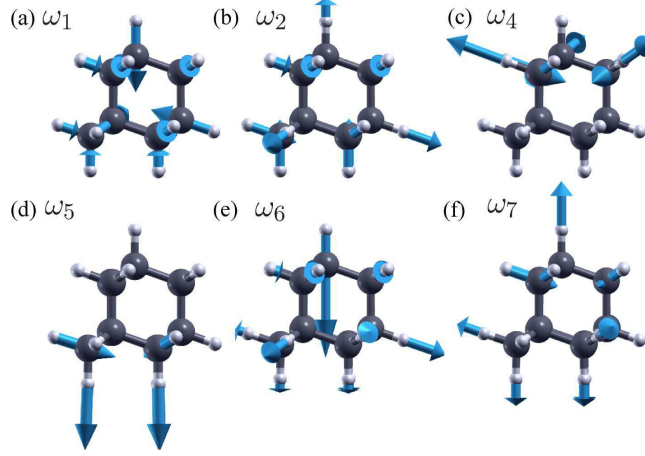


FIG. 3. (Color online) Eigendisplacement vectors of (a) ω_1 , (b) ω_2 , (c) ω_4 , (d) ω_5 , (e) ω_6 , and (f) ω_7 modes of an isolated adamantane molecule (notation is from Table II). Gray and white spheres represent carbon and hydrogen atoms, respectively. Blue arrows indicate the displacements of the atoms (mostly hydrogen atoms). Some of the atoms and eigendisplacements are overlapping since the molecule is shown from a high-symmetry direction.

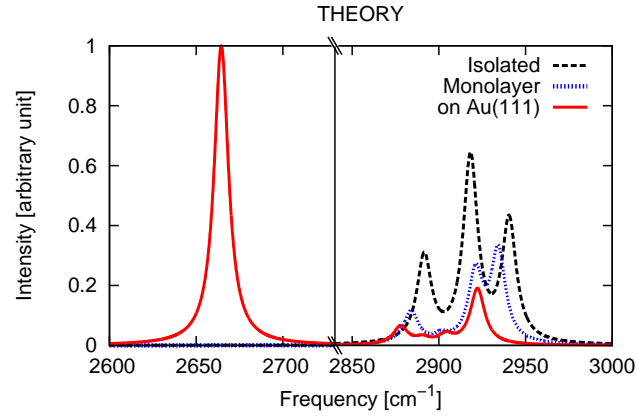


FIG. 4. (Color online) Calculated IR spectrum of an isolated adamantane molecule (black dashed line), an adamantane monolayer (blue dotted line), and an adamantane monolayer on Au(111) (red solid line). The IR spectra are displayed in arbitrary units (chosen so that the intensity of the IR peak around 2650 cm^{-1} equals 1.0). The black vertical line in the figure separates lower and higher frequency regimes (there are no IR active modes in the intermediate regime between 2730 and 2840 cm^{-1}). Here we show only the IR spectra close to the C–H stretching mode frequencies (the closest IR mode not corresponding to C–H stretching is below 1500 cm^{-1}).

TABLE III. Calculated vibrational frequencies (in cm^{-1}) and phonon effective charges Q^z (in elementary charge e) of an adamantane monolayer. We label monolayer phonon modes by ω_1^{M} – ω_6^{M} with one label corresponding to one irreducible representation (irrep). Norm of the overlap between gas phase phonon eigenvector ($\langle u_j |$) and monolayer phonon eigenvector ($|u_i^{\text{M}}\rangle$) is also shown, indicating nature of the hybridization of the gas phase phonons into the monolayer phase phonons. In the table we neglect all overlaps whose norm is smaller than 0.1.

	Gas phase overlap							Irrep	Frequency	Q^z
	ω_1	ω_2	ω_3	ω_4	ω_5	ω_6	ω_7			
ω_1^{M}	0.36	0.63	.	A ₁	2921	0.19
ω_2^{M}	.	0.95	A ₁	2879	0.03
ω_3^{M}	.	.	.	0.99	.	.	.	A ₂	2931	-
ω_4^{M}	0.90	.	.	A ₁	2934	0.22
ω_5^{M}	0.58	0.33	.	A ₁	2902	0.06
ω_6^{M}	0.94	A ₁	2884	0.13

Placing adamantane in the monolayer arrangement (see Sec. III A) lowers the symmetry of the system from T_d (in the gas phase) to C_{3v} . This symmetry reduction is followed by splitting of the threefold degenerate T_2 representation (in T_d) to a twofold E representation and a onefold A_1 representation. The basis functions of the E representation are x and y , therefore they have no IR activity in the z direction (perpendicular to the monolayer). In contrast, the modes with A_1 representation are active along the z direction. In addition, symmetry reduction to the adamantane monolayer splits the T_1 representation into E and A_2 , both of which are IR inactive in the z direction (E is active in x and y). Therefore, the adamantane monolayer has in total five C–H stretching modes that are IR active along the z direction. We label these five modes corresponding to the A_1 representation with ω_1^{M} , ω_2^{M} , ω_4^{M} , ω_5^{M} , and ω_6^{M} .

The blue dashed line in Fig. 4 shows the calculated IR spectrum of the adamantane monolayer. The changes in the IR spectrum of the adamantane monolayer compared to

the single molecule are presented in more detail in Fig. 5 and in Table III. Figure 5 shows interpolated IR spectra between a single molecule and a molecular monolayer case (using the interpolation method described in Sec. III B). Table III shows the calculated vibrational frequencies, phonon effective charges, and inner products between phonon eigenvectors of gas and monolayer adamantane.

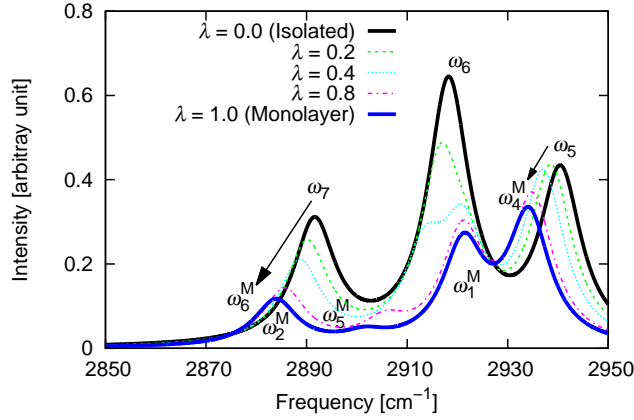


FIG. 5. (Color online) Interpolated IR spectra between the single molecule adamantane (solid black line) and the adamantane monolayer (solid blue line). The dashed ($\lambda = 0.2$), dotted ($\lambda = 0.4$), and chain ($\lambda = 0.8$) lines are interpolated spectra between two cases (using techniques from Sec. III B). The arrows indicate the peaks evolution from the isolated molecule case to the monolayer case.

From Fig. 5 and the inner products in Table III, we find that there is one-to-one correspondence between the ω_2 , ω_4 , ω_5 , ω_7 modes of a single molecule adamantane phase and the ω_2^M , ω_3^M , ω_4^M , and ω_6^M modes of the monolayer adamantane phase, respectively. This correspondence is also evident in the similarity of the phonon eigendisplacement vectors of these two phases (compare Figs. 3(b), (c), (d), (f) and Figs. 6(b), (c), (d), (f)). Three of these modes (ω_2 , ω_5 , and ω_7) are redshifted by about 10 cm^{-1} in the monolayer phase (see arrows in Fig. 5) which is close to the redshifts found in the solid phase diamondoids.⁵ The IR inactive mode ω_4 is redshifted by 7 cm^{-1} in the monolayer phase.

The remaining IR active C–H stretching modes in the adamantane monolayer (ω_1^M and ω_5^M) result from a strong mixing of the ω_1 and ω_6 modes in the gas phase (the inner products shown in Table III are between 0.33 and 0.63) which also affects their eigendisplacement patterns (compare Figs. 3(a) and (e) and Figs. 6(a) and (e)). In addition, the ω_5^M mode is redshifted by about 20 cm^{-1} with respect to the ω_1 and ω_6 mode in the gas phase.

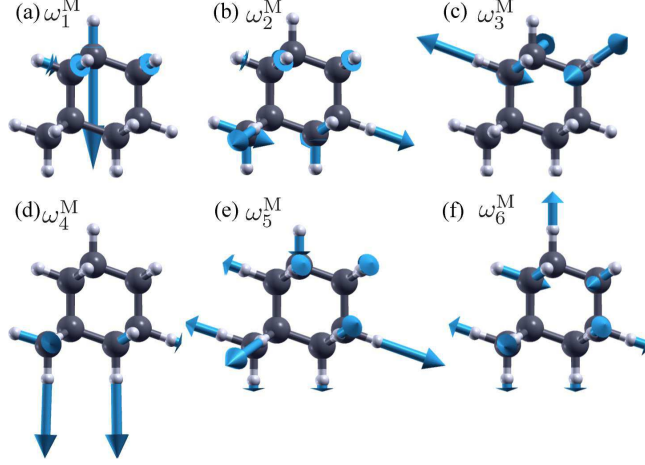


FIG. 6. (Color online) Phonon eigendisplacement vectors of (a) ω_1^M , (b) ω_2^M , (c) ω_3^M , (d) ω_4^M , (e) ω_5^M , and (f) ω_6^M modes of an adamantane monolayer without a gold substrate.

3. Monolayer on Au(111)

Finally, we study the vibrational properties of the adamantane monolayer on a Au(111) surface. Introduction of the Au(111) surface further reduces the symmetry of the system from C_{3v} (in the monolayer) to C_3 . Due to symmetry reductions, both the IR active A_1 mode and the IR inactive A_2 mode having C_{3v} symmetry (monolayer) are changed to the IR active A representation having C_3 symmetry. The IR inactive E modes, remains inactive in the C_3 symmetry along the z direction. The red solid line in Fig. 4 shows the calculated IR spectrum of a molecular monolayer on a gold substrate. Vibrational frequencies and phonon effective charges are shown in Table IV. The most notable difference compared to the spectrum of the isolated adamantane monolayer and gas phase molecule is the significant redshift of one of the modes ω_6^{Au} (to 2664 cm^{-1}) with a sizable increase in the phonon effective charge ($0.40 e$).

Figure 7 shows the interpolated IR spectra between the isolated monolayer case and the monolayer on Au(111). This analysis shows that the ω_1^{Au} mode is nearly unaffected by the Au(111) substrate as it originates from the stretching of a topmost C–H bond, relatively far from the Au(111) surface. In fact, the eigendisplacement vectors of the ω_1^{Au} mode and ω_1^M mode are nearly the same (compare Fig. 6(a) and Fig. 8(a)).

Interpolation analysis of the remaining IR peaks is quite involved in this case. Therefore we turn to the analysis of the inner products of the phonon modes in the isolated monolayer and the monolayer of on Au(111). These inner products are shown in Table IV. From this

TABLE IV. Vibrational frequencies (in cm^{-1}), phonon effective charges Q^z (in elementary charge e), and inner products of C–H stretching modes of adamantane molecules on a Au(111) surface. Norm of the overlap between adamantane monolayer phase phonon eigenvector ($\langle u_j^{\text{M}} |$) and monolayer on gold phonon eigenvector ($|u_i^{\text{Au}}\rangle$) is also shown, indicating the nature of the hybridization of the gas phase phonons into the monolayer phase phonons. In the Table we neglect all overlaps whose norm is smaller than 0.1.

	Monolayer phase overlap						Irrep	Frequency	Q^z
	ω_1^{M}	ω_2^{M}	ω_3^{M}	ω_4^{M}	ω_5^{M}	ω_6^{M}			
ω_1^{Au}	1.00	A	2922	0.17
ω_2^{Au}	.	0.35	.	.	0.27	0.33	A	2878	0.10
ω_3^{Au}	.	.	1.00	.	.	.	A	2935	0.01
ω_4^{Au}	.	0.34	.	0.21	0.42	.	A	2904	0.06
ω_5^{Au}	0.29	0.63	A	2891	0.07
ω_6^{Au}	.	0.27	.	0.70	.	.	A	2664	0.40

table we again confirm that the ω_1^{Au} mode originates from the ω_1^{M} mode. In addition, we find that the ω_3^{Au} mode has one-to-one correspondence with the ω_3^{M} mode.

For the remaining IR active modes (ω_2^{Au} , ω_4^{Au} , ω_5^{Au} , and ω_6^{Au}) we find strong influence by the monolayer-substrate interaction. Analyzing Table IV reveals that the ω_2^{Au} mode of adamantane on the Au(111) substrate is a mixture of the ω_2^{M} , ω_5^{M} , and ω_6^{M} modes of the isolated monolayer phase. Similarly, the ω_4^{Au} mode is composed of the ω_2^{M} , ω_4^{M} , and ω_5^{M} modes, while the ω_5^{Au} mode comes mostly from the ω_6^{M} mode with some admixture of the ω_5^{M} mode. The IR intensity of modes ω_2^{Au} , ω_4^{Au} and ω_5^{Au} are relatively small since these modes include only a small amount of C–H bond stretching perpendicular to the surface (see phonon eigendisplacements in Fig. 8).

On the other hand, Table IV shows a rather remarkable change in the frequency and IR intensity of the ω_6^{Au} mode. This mode is a mixture of the ω_4^{M} (2934 cm^{-1}) and ω_2^{M} (2879 cm^{-1}) modes of the isolated monolayer phase and its frequency is red shifted to

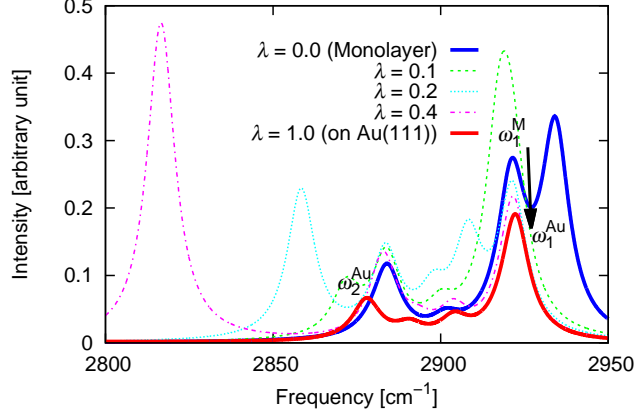


FIG. 7. (Color online) Interpolated IR spectra going from an isolated molecular monolayer to a monolayer on Au(111). The blue solid line shows the IR spectrum of the isolated molecular monolayer, while the red solid line shows the IR spectrum of the monolayer on the Au(111) substrate. The dashed ($\lambda = 0.1$), dotted ($\lambda = 0.2$), and chain ($\lambda = 0.4$) lines show an interpolated spectra between the two cases. The arrow shows the transition from ω_1^M to ω_1^{Au} . We also indicate the peak position of the relatively weak ω_2^{Au} mode. The severely redshifted peak ω_6^{Au} is not shown in this figure (see left panel of Fig. 4.)

2664 cm^{-1} . Furthermore, its IR intensity is increased from $0.05 e^2$ to $0.16 e^2$ (effective charge in Table IV changes from $0.22 e$ to $0.40 e$) compared to the ω_4^M mode. The ω_6^{Au} mode consists of the in-phase perpendicular vibration of the three bottom hydrogen atoms near the Au(111) surface (see Fig. 8(f)), therefore it is not unexpected that this mode will be significantly affected by the Au(111) surface. Comparison of the charge density of the isolated adamantane monolayer to the charge density of the monolayer on the Au(111) surface reveals that the molecule-surface interaction reduces the electron charge density on the adamantane C–H bonds. We speculate that this reduction of charge density within the C–H bonds is responsible for the decrease in the ω_6^{Au} mode frequency as well as increase of its effective charge.

C. Comparison of theory and experiment

Figure 9 shows a comparison of the experimental (green line) and theoretical (dashed blue line) IR spectra for an adamantane monolayer on the Au(111) surface. We find good

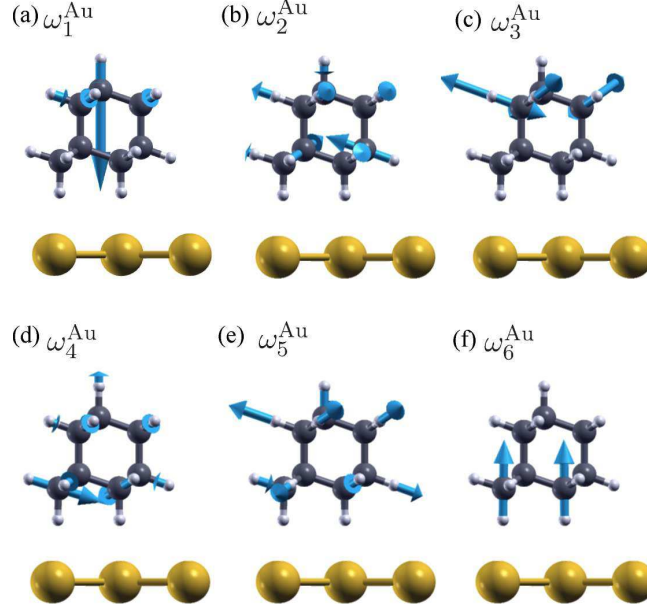


FIG. 8. (Color online) Eigendisplacement vectors of (a) ω_1^{Au} , (b) ω_2^{Au} , (c) ω_3^{Au} , (d) ω_4^{Au} , (e) ω_5^{Au} , and (f) ω_6^{Au} modes of an adamantane monolayer on the Au(111) surface. Yellow spheres illustrate Au atoms in the topmost layer of the Au(111) surface.

qualitative agreement between the two spectra, both in the peak position and in their relative intensities (the experimental vertical scale is chosen so that the peak height at 2846 cm^{-1} matches the theoretical peak height at 2851 cm^{-1}). Agreement is even better after applying a correction to the calculated phonon frequencies (red line in Fig. 9) as we describe below in Sec. IV C 1.

We assign the relatively large experimentally obtained IR peak at 2912 cm^{-1} to the theoretically obtained ω_1^{Au} mode (2922 cm^{-1} , corrected frequency 2914 cm^{-1} , phonon effective charge $0.17 e$). Furthermore, we assign the relatively weaker mode at 2846 cm^{-1} to the theoretically obtained ω_2^{Au} mode (2878 cm^{-1} , corrected frequency 2851 cm^{-1} , phonon effective charge $0.10 e$). Remaining features in the experimental data (green line in Fig. 9) are not reproducible and therefore cannot be reliably assigned to the additional IR phonon modes. This is consistent with our theory, as the remaining IR active modes ω_3^{Au} , ω_4^{Au} , and ω_5^{Au} have a much smaller phonon effective charge (from 0.01 to $0.07 e$).

Finally, our calculation predicts the existence of a significantly redshifted IR active mode ω_6^{Au} at 2664 cm^{-1} (corrected value is 2644 cm^{-1}) with a large phonon effective charge ($0.40 e$). Although the frequency of this mode is currently outside of our experimentally attainable

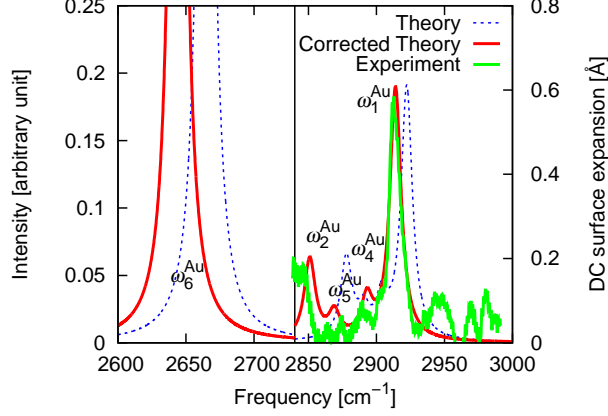


FIG. 9. (Color online) Uncorrected (blue dashed line) and corrected (red solid line) theoretical IR spectra and experimentally observed IR spectrum (green solid line). The frequency region between 2730 cm^{-1} and 2840 cm^{-1} is not shown. The vertical scale is chosen so that the theoretical and experimental peaks around 2850 cm^{-1} have almost the same height. Left and right vertical axes correspond to theoretical and experimental IR intensity. Corrected theoretical values of ω_1^{Au} , ω_2^{Au} , ω_4^{Au} , ω_5^{Au} , and ω_6^{Au} modes are 2914 , 2851 , 2893 , 2869 , and 2644 cm^{-1} , respectively.

frequency range (from 2840 to 2990 cm^{-1}), we expect that it will be accessible to future experimental probing.

1. Correction of the dynamical matrix

Here we present the method we use to correct the DFT-LDA IR spectrum of the adamantane monolayer on the Au(111) substrate (red line in Fig. 9). First we obtain the correction D^{corr} to the calculated dynamical matrix of the adamantane *gas* phase so that it exactly reproduces the experimentally measured frequencies of adamantane gas and solution phase,

$$D^{\text{corr}} = \sum_i (\Delta_i^2 - 2\omega_i \Delta_i) |u_i\rangle \langle u_i|. \quad (5)$$

Here ω_i and $|u_i\rangle$ are the phonon frequencies and eigenvectors of the original dynamical matrix, while Δ_i is the difference between the computed and the measured adamantane gas and solution phase frequency. In the second step, we add this same correction matrix D^{corr} to the dynamical matrix of the adamantane monolayer on the Au(111) surface. Finally, we use the eigenvalues and eigenvectors of the corrected dynamical matrix to compute the

corrected IR spectrum.

Our correction procedures improve the agreement of the calculated IR spectrum of adamantane on the Au(111) surface with the experimental spectrum (see Fig. 9). The theoretical peak position of the ω_1^{Au} mode is redshifted by 8 cm^{-1} (from 2922 cm^{-1} to 2914 cm^{-1}) and sits closer to the experimental peak position ($2913 \pm 1 \text{ cm}^{-1}$). Similarly, the ω_2^{Au} mode is redshifted by 27 cm^{-1} (from 2878 cm^{-1} to 2851 cm^{-1}), again closer to the experimental value ($2846 \pm 2 \text{ cm}^{-1}$).

V. SUMMARY AND CONCLUSIONS

Our work combining IRSTM¹⁴ measurements and *ab initio* calculation of the IR spectrum of an adamantane monolayer on Au(111) demonstrates the complex nature of *adamantane–adamantane* and *adamantane–gold* interactions. In Sec. IV B we have described in detail the effect of each of these interactions on the mixing (hybridization) of adamantane vibrational modes, the changes in their frequencies, and the IR intensities. Figure 10 summarizes our main results. The black dashed line in Fig. 10 shows the calculated isolated adamantane gas phase IR spectrum, while the red line shows the severely modified spectrum of the adamantane monolayer on the Au(111) surface. The green line shows the experimental spectrum of an adamantane submonolayer on Au(111).

The IR spectrum of the isolated adamantane molecule (black dashed line in Fig. 10) consists of three IR active C–H stretching modes ($\omega_5, \omega_6, \omega_7$). The *adamantane–adamantane* interaction (packing effect) reduces the IR intensity of one of these modes (ω_6) by a factor of 3.5. On the other hand, the *adamantane–gold* interaction severely redshifts the gas phase ω_5 mode (by 276 cm^{-1}), and increases its IR intensity by a factor of 2.6. In addition, both ω_5 and ω_6 are hybridized with IR inactive gas phase modes (ω_2 and ω_1 respectively). See Sections IV B 2, IV B 3 and Tables III, IV for more details.

In conclusion, we expect that these techniques can be used to study intermolecular and molecule–substrate effects of other molecular systems, including the use of other metallic substrates. In particular, we expect that the IR intensity reduction of the gas phase ω_6 mode (or equivalent, for other molecules) can be used as a direct measure of intermolecular interactions. Similarly, the increase in the IR intensity and the redshift of the ω_5 mode can be used as a direct measure of molecule–substrate interactions.

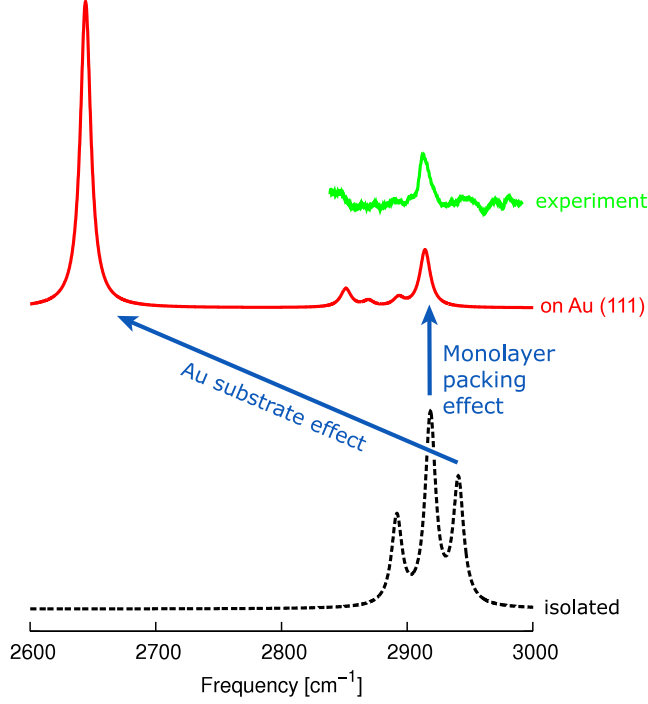


FIG. 10. (Color online) Summary of our main results. There are three IR active C–H stretching modes in the isolated (gas phase) adamantane molecule (black dashed line). The interaction between the neighboring adamantane molecules in the monolayer (packing effect) reduces the IR intensity of the central IR active mode by a factor of 3.5. The interaction between the monolayer and the Au(111) surface (Au substrate effect) reduces the highest frequency gas phase mode by 276 cm^{-1} and it increases its IR intensity by a factor of 2.6. The remaining third IR active gas phase mode is affected both by the Au(111) substrate and by the packing effect. See Sec. IV B for more detailed analysis. The calculated IR spectrum of an adamantane monolayer on Au(111) is shown with a red line, while the experimental spectrum is shown with a green line.

ACKNOWLEDGMENTS

Computational resources were provided by the DOE at Lawrence Berkeley National Laboratory’s NERSC facility. Numerical calculations were also carried out on the TSUBAME2.0 supercomputer in the Tokyo Institute of Technology. Theoretical part of the work was supported by NSF Grant No. DMR-10-1006184 (structural determination) and by the Nanomachines Program at the Lawrence Berkeley National Lab funded by the office of Basic Energy Sciences, DOE under Contract No. DE-AC02-05CH11231 (infrared spectra simulations and analyses). The Experimental part of the study was supported by the Nanomachines

Program of the Office of Basic Energy Sciences, Materials Sciences and Engineering Division, U.S. Department of Energy under Contract No. DE-AC02-05CH11231 (STM measurements) and by the Department of Energy Early Career Award de-sc0003949 (development of IR laser source). YS acknowledges financial support from Japan Society for the Promotion of Science. RBC acknowledges financial support from Brazilian agencies CNPq, FAPERJ, INCT - Nanomateriais de Carbono and Rede de Pesquisa e Instrumentação em Nano-Espectroscopia Óptica. SGL acknowledges support of a Simons Foundation Fellowship in Theoretical Physics.

-
- ¹ N. D. Drummond, A. J. Williamson, R. J. Needs, and G. Galli, *Phys. Rev. Lett.* **95**, 096801 (2005).
 - ² W. L. Yang, J. D. Fabbri, T. M. Willey, J. R. I. Lee, J. E. Dahl, R. M. K. Carlson, P. R. Schreiner, A. A. Fokin, B. A. Tkachenko, N. A. Fokina, W. Meevasana, N. Mannella, K. Tanaka, X. J. Zhou, T. van Buuren, M. A. Kelly, Z. Hussain, N. A. Melosh, and Z.-X. Shen, *Science* **316**, 1460 (2007).
 - ³ Y. Wang, E. Kioupakis, X. Lu, D. Wegner, R. Yamachika, J. E. Dahl, R. M. K. Carlson, S. G. Louie, and M. F. Crommie, *Nat. Mater.* **7**, 38 (2008).
 - ⁴ D. F. Blake, F. Freund, K. F. M. Krishnan, C. J. Echer, R. Shipp, T. E. Bunch, A. G. Tielens, R. J. Lipari, C. J. D. Hetherington, and S. Chang, *Nature (London)* **332**, 611 (1988).
 - ⁵ O. Pirali, M. Vervloet, J. E. Dahl, R. M. K. Carlson, A. G. G. M. Tielens, and J. Oomens, *Astrophys. J.* **661**, 919 (2007).
 - ⁶ R. Bailey, *Spectrochimica Acta Part A: Molecular Spectroscopy* **27**, 1447 (1971).
 - ⁷ T. J. Broxton, L. W. Deady, M. Kendall, and R. D. Topsom, *Appl. Spectrosc.* **25**, 600 (1971).
 - ⁸ P.-J. Wu, L. Hsu, and D. A. Dows, *J. Chem. Phys.* **54**, 2714 (1971).
 - ⁹ R. M. Corn, V. L. Shannon, R. G. Snyder, and H. L. Strauss, *J. Chem. Phys.* **81**, 5231 (1984).
 - ¹⁰ L. Bisticic, G. Baranovic, and K. Mlinaricmajerski, *Spectrochim. Acta, Part A* **51**, 1643 (1995).
 - ¹¹ G. Szasz and A. Kovacs, *Mol. Phys.* **96**, 161 (1999).
 - ¹² J. Jensen, *Spectrochim. Acta, Part A* **60**, 1895 (2004).
 - ¹³ O. Pirali, V. Boudon, J. Oomens, and M. Vervloet, *J. Chem. Phys.* **136**, 024310 (2012).

- ¹⁴ I. V. Pechenezhskiy, X. Hong, G. D. Nguyen, J. E. P. Dahl, R. M. K. Carlson, F. Wang, and M. F. Crommie, *Phys. Rev. Lett.* **111**, 126101 (2013).
- ¹⁵ T. Kitagawa, Y. Idomoto, H. Matsubara, D. Hobara, T. Kakiuchi, T. Okazaki, and K. Komatsu, *J. Org. Chem.* **71**, 1362 (2006).
- ¹⁶ X. Hong, X. Shen, M. Gong, and F. Wang, *Opt. Lett.* **37**, 4982 (2012).
- ¹⁷ P. Hohenberg and W. Kohn, *Phys. Rev.* **136**, 864 (1964).
- ¹⁸ W. Kohn and L. J. Sham, *Phys. Rev.* **140**, 1133 (1965).
- ¹⁹ D. M. Ceperley and B. J. Alder, *Phys. Rev. Lett.* **45**, 566 (1980).
- ²⁰ J. P. Perdew and A. Zunger, *Phys. Rev. B* **23**, 5048 (1981).
- ²¹ D. Vanderbilt, *Phys. Rev. B* **41**, 7892 (1990).
- ²² P. Giannozzi, S. Baroni, N. Bonini, M. Calandra, R. Car, C. Cavazzoni, D. Ceresoli, G. L. Chiarotti, M. Cococcioni, I. Dabo, A. Dal Corso, S. de Gironcoli, S. Fabris, G. Fratesi, R. Gebauer, U. Gerstmann, C. Gougoussis, A. Kokalj, M. Lazzeri, L. Martin-Samos, N. Marzari, F. Mauri, R. Mazzarello, S. Paolini, A. Pasquarello, L. Paulatto, C. Sbraccia, S. Scandolo, G. Sclauszero, A. P. Seitsonen, A. Smogunov, P. Umari, and R. M. Wentzcovitch, *J. Phys. Condens. Matter* **21**, 5502 (2009).
- ²³ A. Kokalj, *Comput. Mater. Sci.* **28**, 155 (2003).
- ²⁴ M. L. Cohen, M. Schlüter, J. R. Chelikowsky, and S. G. Louie, *Phys. Rev. B* **12**, 5575 (1975).
- ²⁵ H. Rydberg, M. Dion, N. Jacobson, E. Schröder, P. Hyldgaard, S. I. Simak, D. C. Langreth, and B. I. Lundqvist, *Phys. Rev. Lett.* **91**, 126402 (2003).
- ²⁶ K. Lee, É. D. Murray, L. Kong, B. I. Lundqvist, and D. C. Langreth, *Phys. Rev. B* **82**, 081101 (2010).
- ²⁷ V. R. Cooper, *Phys. Rev. B* **81**, 161104 (2010).
- ²⁸ I. Hamada and M. Tsukada, *Phys. Rev. B* **83**, 245437 (2011).
- ²⁹ G. Li, I. Tamblyn, V. R. Cooper, H.-J. Gao, and J. B. Neaton, *Phys. Rev. B* **85**, 121409 (2012).
- ³⁰ S. Baroni, S. de Gironcoli, A. dal Corso, and P. Giannozzi, *Rev. Mod. Phys.* **73**, 515 (2001).
- ³¹ D. Porezag and M. R. Pederson, *Phys. Rev. B* **54**, 7830 (1996).
- ³² R. G. Greenler, *J. Chem. Phys.* **44**, 310 (1966).
- ³³ R. Hexter and M. G. Albrecht, *Spectrochim. Acta, Part A* **35**, 233 (1979).
- ³⁴ N. Sheppard and J. Erkelens, *Appl. Spectrosc.* **38**, 471 (1984).